

Final Report

Dong Heon Han¹

October 6, 2025

¹Robotics Department, University of Michigan, PhD Program in Robotics. (unique name: dongheon)

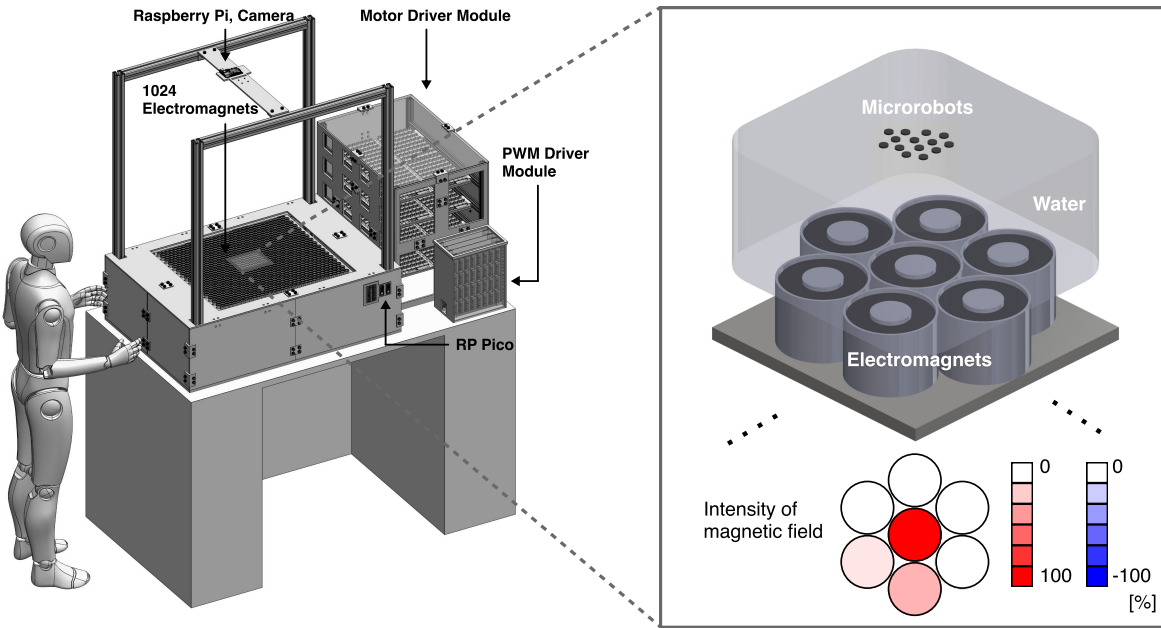


Figure 1: Depiction of the magnetic microrobot swarm control platform (2ft x 2ft arena available for the microrobots to move on) with a human standing beside. The platform has three main parts: the workspace, the main module with the electromagnets, and two towers that each hold the motor drivers and PWM drivers. In addition, it schematically shows how seven electromagnets are controlled in terms of intensity and magnetic orientation (red and blue).

1 Introduction and background

Microrobots are being developed as tools for accessing sub-millimeter and other confined regions that conventional instruments cannot reach [1, 2]. Robots at millimeter–micrometer scales can access enclosed environments, but their limited volume makes it difficult to incorporate onboard actuators, electronics, or power systems [3]. To operate in such constrained domains, these robots typically rely on external stimuli, including light [4–6], acoustics [7, 8], and magnetic fields [9–11]. As a result, recent studies have explored their use in micro-fabrication [12, 13], bio-manipulation [14], sensing [15], and targeted minimally invasive therapies [16].

However, as robot size decreases and task complexity increases, individual microrobots face structural and functional constraints. Their limited size restricts onboard electronics, sensing, and energy storage, making autonomous operation challenging. Although MEMS, CMOS, and custom PCB approaches have demonstrated promising integrated actuation or sensing, practical power delivery and autonomy remain major bottlenecks at small scales [17–20].

To overcome these limitations, one can consider microrobotic systems that operate without onboard electronics, actuators, or energy storage and instead rely entirely on externally applied magnetic fields. **First**, magnetic actuation provides a practical and reliable alternative because magnetic fields penetrate biological tissue and microfluidic environments, enabling controlled motion in confined and densely structured spaces [21, 22]. This capability supports biomedical applications such as targeted intervention and micro-fabrication tasks that require precise manipulation within complex geometries. **Second**, magnetically actuated robots are compatible with rapid and scalable manufacturing. In contrast, highly integrated robots that rely on onboard actuation require high-resolution fabrication,

which increases cost and process time and reduces practicality for complex single-robot designs. Indeed, many existing systems relying on onboard capability remain tethered or require external energy transmission via wired or optical links [23–26]. Magnetic actuation avoids these constraints entirely, enabling untethered operation without embedded power or computation. Together, these factors position magnetic actuation as a particularly powerful and scalable approach for microrobotic systems.

Magnetic actuation enables scalable untethered operation, but individual microrobots remain functionally constrained, making collective control essential for more advanced behaviors. These robots cannot carry onboard sensing or computation, so they cannot coordinate through traditional multi-robot strategies. Instead, global magnetic fields induce magnetic, hydrodynamic, and capillary interactions that govern their behavior and drive self-organization without onboard intelligence. Prior magnetic microrobot systems have shown that these interactions can generate diverse collective modes, including vortices, chains, lattices, and transitions between gas-like, rotational, and translational states [27–29]. These emergent modes enable capabilities inaccessible to individual robots, such as cooperative transport, reconfigurable assembly, adaptive morphology, and programmable spatial distributions. Heterogeneity in robot size or geometry can further introduce asymmetric interactions, enabling behaviors such as controlled aggregation and dispersion, anisotropic deformation, and selective manipulation of external objects [30].

However, global magnetic fields apply the same actuation to all robots, limiting the ability to create spatially distinct behaviors or programmable patterns. In contrast, localized magnetic fields offer spatially selective control and reconfiguration, enabling more complex patterns, time-varying formations, and cooperative manipulation with higher versatility [10, 31]. These considerations motivate the need for scalable methods that combine global coordination with localized magnetic control to program collective behavior in dense microrobot systems.

While prior work has demonstrated localized magnetic control, existing systems operate with a small number of coils or discrete magnetic sources, limiting the spatial resolution and scalability of programmable magnetic inputs. As a result, collective behaviors have been explored only at modest population sizes and with relatively coarse field patterns. In contrast, we aim to investigate magnetic microrobot collectives under far higher actuation density by increasing the number of independently controlled electromagnets to the pixel level. This approach enables the generation of rich, spatially structured magnetic fields that can drive significantly more complex collective behaviors. As a first step toward this goal, we study the fundamental control capabilities of such high-resolution magnetic inputs using an air–water interface testbed, targeting reconfigurable behaviors in collectives of 10,000 robots or more as a proof of concept (Fig.1).

2 Research scope (in the Microrobotics course)

The first aim of this project is to design and fabricate a real-time hardware platform capable of controlling 1024 independent electromagnetic channels simultaneously (Fig. 1). The platform will implement fully parallelized PWM actuation with deterministic timing and sub-millisecond update latency, extending prior localized magnetic control strategies [10] to a much larger and spatially resolved electromagnet array. A hierarchical control architecture integrates low-level I²C communication for synchronized driver operation with high-level coordination through an RP Pico–RP4 interface, enabling fast and reliable actuation.

The second aim is to fabricate low-cost, mass-producible microrobots in the form of magnetically dipolar microdisks. This involves establishing scalable microfabrication procedures with high geometric precision, developing a permanent-magnet-based magnetization workflow that produces stable and consistent dipole alignment without specialized equipment, and optimizing the microdisk geometry to enhance magnetic torque response under applied fields.

The third aim is to develop fundamental control capabilities on the 1024-channel electromagnetic platform. This includes establishing reliable object manipulation routines, characterizing how locally varying magnetic inputs generate emergent collective motion, and demonstrating precise trajectory tracking and formation shaping through spatially programmable magnetic fields. Together, these developments will form the basis for large-scale magnetic control and provide a platform for exploring multi-agent behaviors within a fully programmable electromagnetic environment.

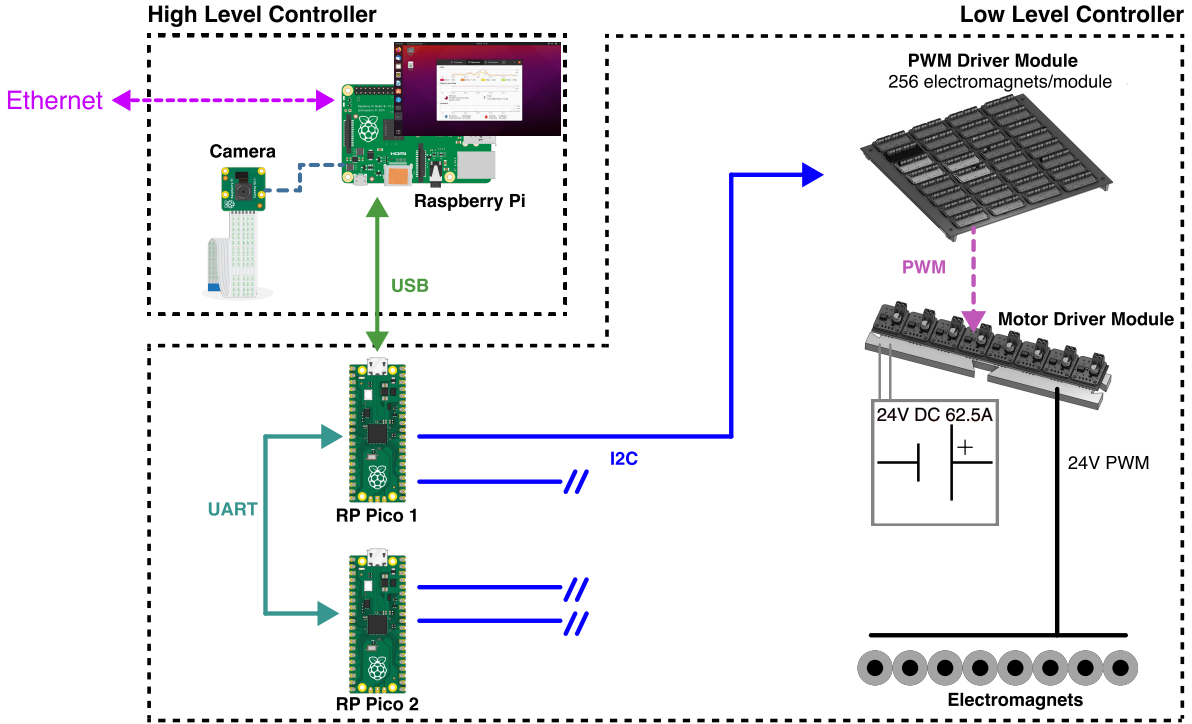


Figure 2: The high level and low level controllers and the connections between them. The two RP Pico (Raspberry Pi Pico) boards communicate through an RS485 protocol implemented over UART, which enables fast and reliable data transfer between the microcontrollers. Each microcontroller communicates with its associated PWM driver module through an I2C interface. The PWM driver module receives the commanded values and rapidly switches the H bridge motor driver module on and off. The motor driver module is connected to the electromagnets and generates the magnetic field strengths required for actuation.

3 Methods and approach

Fig. 1 illustrates the layout and approximate scale of all devices in the experimental platform except for the computer. The purpose of this overall design is to sense the microrobot collective through overhead vision and to drive the robots in desired directions by regulating the one thousand twenty four electromagnets. Each electromagnet can be activated in the positive or negative direction, and each direction provides sixteen discrete control levels that adjust the magnetic strength. Fig. 2 provides a schematic representation of the system. The architecture consists of two layers referred to as the low level and the high level. The low level receives the magnetic strength commands for each time step in the form of 1024 data values represented as binary numbers and its only function is to output these values to the corresponding electromagnets. The high level operates together with the overhead camera and determines the magnetic input at every instant. All intelligence of the system resides here. The high level performs closed loop control of the collective, estimates and regulates the group motion, and computes desired trajectories for both individual robots and larger formations. In this sense it serves as the brain of the platform, coordinating sensing, control, and real time decision making.

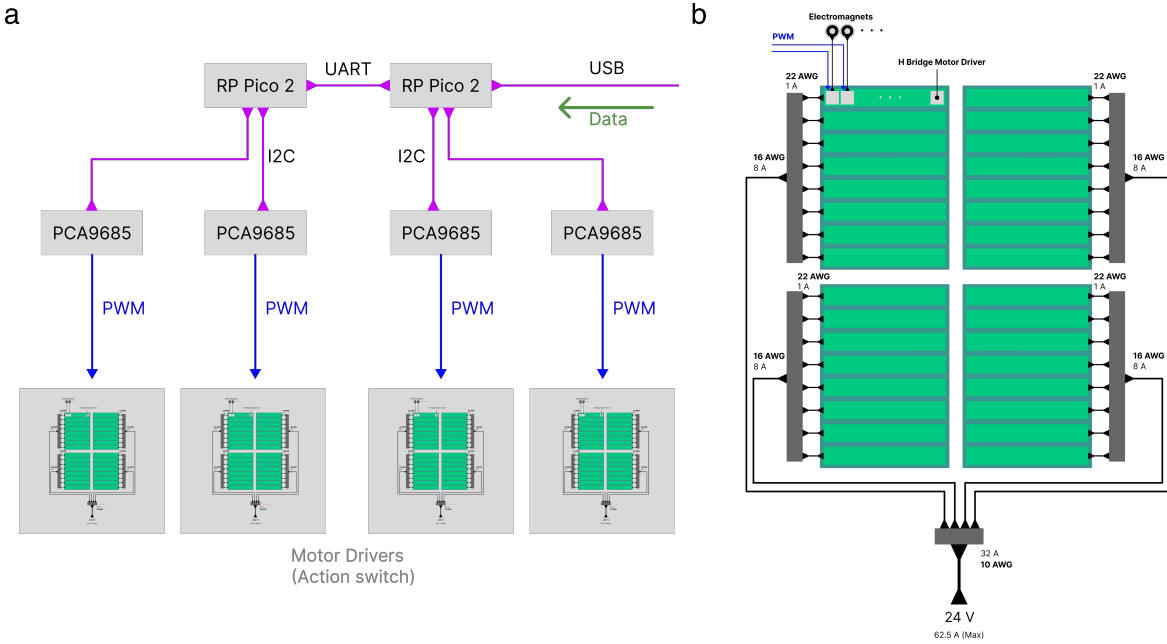


Figure 3: Overview of the low-level control and power-distribution architecture. (a) Hardware elements used for low-level control, illustrating the communication flow between RP Pico boards, RS485 links, and the I²C interfaces that drive the PWM modules. The diagram highlights the direction of data transmission and the structure of the command pipeline used to update all electromagnets in real time. (b) Detailed wiring schematic of the DRV8871 motor-driver modules, showing how power lines are routed to each module, the gauge of the conductors, and the safety components integrated into the system. Fuse ratings, wire thickness, and current capacities are indicated to emphasize the safety considerations used in distributing 24 V power across the electromagnet array.

3.1 Low level control and communication

The high level controller outputs a continuous valued command vector

$$\mathbf{x} = (x^1, \dots, x^{1024})^\top \in [0, 1]^{1024} \subset \mathbb{R}^{1024},$$

where x^i is the normalized magnetic strength requested for the i -th electromagnet. This vector is quantized and then encoded into a binary pattern that can be sent to the low level hardware:

$$\mathbf{x} \in [0, 1]^{1024} \xrightarrow{Q} \hat{\mathbf{x}} \in \mathcal{L}^{1024} \xrightarrow{\text{encode}} \mathbf{b} \in \{0, 1\}^{4096}, \quad \mathcal{L} = \left\{0, \frac{1}{15}, \frac{2}{15}, \dots, \frac{15}{15}\right\}.$$

The quantizer Q maps each entry to the nearest element of \mathcal{L} ,

$$\hat{x}^i = Q(x^i) = \frac{1}{15} \text{round}(15x^i),$$

so that \hat{x}^i takes one of 16 discrete levels between 0 and 1. Each quantized value \hat{x}^i is then encoded as a 4 bit unsigned integer in $\{0, \dots, 15\}$, and stacking all 4 bit words produces the binary vector $\mathbf{b} \in \{0, 1\}^{4096}$. The sign of the commanded current is handled separately by the DRV8871 H bridge motor drivers, so the binary pattern \mathbf{b} represents only the magnitude of the duty cycle for the 1024 electromagnets.

Figure 3(a) illustrates how this data flows through the low level hardware. At each control step the high level sends the vector \mathbf{b} to RP Pico 2, which receives the real time state of all 1024 magnets. Here the state refers to the duty cycles that determine whether each electromagnet is effectively off or on with a given strength; these duty cycles can later be mapped to magnetic field magnitudes for each electromagnet model. RP Pico 2 keeps the full command but forwards half of the data to RP Pico 1. In other words, RP Pico 2 and RP Pico 1 each hold the command for 512 magnets.

The communication between RP Pico 1 and RP Pico 2 uses a differential RS485 link implemented over a UART interface. This provides fast and reliable communication even in the presence of electrical

noise introduced by the large number of switching drivers. Each RP Pico then distributes its 512 magnet commands over 2 I²C buses. For each RP Pico, one I²C line (I²C1) carries commands for the first 256 magnets and the second line (I²C2) carries commands for the remaining 256 magnets. Along each I²C line the data are addressed to 32 PWM driver modules. Each address receives 8 command values, so that every module controls 8 DRV8871 H bridge motor driver boards. As shown in Figure 3(b), each DRV8871 motor driver drives a single electromagnet. Because the drivers use an H bridge topology, the polarity of the current through each electromagnet can be reversed and the duty cycle can be modulated at high frequency. The electromagnets themselves are commercial 24 V devices (Uxcell DC24V 2.5KG Force Eelectric Lifting Magnet), so a constant 24 V supply is applied to the motor drivers while the effective magnetic strength is controlled by the duty cycle.

Communication timing analysis We now estimate the theoretical lower bound on the time required to update all 1024 electromagnets once.

The high level must transmit one binary vector \mathbf{b} per control step. The number of magnets and bits per magnet are

$$N_{\text{mag}} = 1024, \quad N_{\text{bits,mag}} = 4,$$

so the payload size is

$$N_{\text{payload}} = N_{\text{mag}} N_{\text{bits,mag}} = 4096 \text{ bits.}$$

USB transfer to RP Pico 2. Let R_{USB} denote the effective USB data rate in bits per second. Then the time to send one command frame is

$$t_{\text{USB}} = \frac{N_{\text{payload}}}{R_{\text{USB}}}.$$

For a full speed link with $R_{\text{USB}} = 12 \times 10^6$ bit/s,

$$t_{\text{USB}} \approx \frac{4096}{12 \times 10^6} \approx 3.4 \times 10^{-4} \text{ s.}$$

RS485 transfer from RP Pico 2 to RP Pico 1. Only half of the payload, corresponding to 512 magnets, is forwarded from RP Pico 2 to RP Pico 1. The forwarded payload therefore has

$$N_{\text{UART}} = 512 \times 4 = 2048 \text{ bits.}$$

If the UART over RS485 runs at rate R_{UART} bit per second, the transfer time is

$$t_{\text{UART}} = \frac{N_{\text{UART}}}{R_{\text{UART}}}.$$

For $R_{\text{UART}} = 10^6$ bit/s,

$$t_{\text{UART}} \approx \frac{2048}{10^6} \approx 2.0 \times 10^{-3} \text{ s.}$$

I²C transfer to PWM driver modules. Each I²C bus serves 32 PWM driver modules and each module receives 8 command values every update. With the PCA9685 operated in its standard 12 bit PWM mode, we can update a block of 8 channels on a given device by writing a starting register address followed by the required register bytes under auto increment. Let B_{dev} denote the number of bytes sent per device in one update, including the address and all PWM registers. A typical choice is $B_{\text{dev}} = 34$ bytes, which covers one command byte plus 4 bytes for each of 8 channels. The number of bits sent to one I²C bus in one full update is then

$$N_{\text{I2C,bus}} = 8 B_{\text{dev}} N_{\text{dev}}, \quad N_{\text{dev}} = 32,$$

so with $B_{\text{dev}} = 34$,

$$N_{\text{I2C,bus}} = 8 \times 34 \times 32 = 8704 \text{ bits.}$$

If the bus is operated in fast mode plus at $R_{\text{I2C}} = 10^6$ bit/s, the time to refresh all devices on one bus is

$$t_{\text{I2C}} = \frac{N_{\text{I2C,bus}}}{R_{\text{I2C}}} \approx \frac{8704}{10^6} \approx 8.7 \times 10^{-3} \text{ s.}$$

RP Pico has 2 independent I²C controllers, so I²C1 and I²C2 can operate in parallel. RP Pico 1 and RP Pico 2 can also operate in parallel, so t_{I2C} is the dominant I²C time for a complete update of all magnets.

End to end bound. Under ideal conditions with perfect pipelining, the dominant contributions to the latency for one global update are therefore

$$t_{\text{USB}} \approx 0.34 \text{ ms}, \quad t_{\text{UART}} \approx 2.0 \text{ ms}, \quad t_{I2C} \approx 8.7 \text{ ms}.$$

A conservative lower bound on the total update time is

$$t_{\text{total}} \approx t_{\text{USB}} + t_{\text{UART}} + t_{I2C} \approx 11 \times 10^{-3} \text{ s},$$

which corresponds to a theoretical maximum update rate of

$$f_{\max} \approx \frac{1}{t_{\text{total}}} \approx 90 \text{ Hz}.$$

In practice additional software and protocol overhead will increase the latency, but this analysis indicates that closed loop collective control in the range of 10 to several 10s of hertz is feasible with the present hardware.

3.2 Power distribution and electrical safety

Fig. 3.b illustrates the power distribution architecture used to drive the electromagnet array. Each electromagnet draws approximately 0.125 A at 24 V when operated at a duty cycle of 100%, with experimental variation of about ± 0.05 A. Since each PWM driver module controls 8 DRV8871 motor drivers, the expected module current is roughly 1.0 A, and in the worst case may reach approximately 1.4 A. Eight electromagnets are wired to their DRV8871 drivers using 22 AWG wire. This gauge is sufficient because each branch carries only the current of a single electromagnet, which remains comfortably below the continuous current rating for 22 AWG copper wire. This rating does not interfere with normal operation but isolates short circuits before significant heating can occur, preventing damage to the driver modules or wiring. Eight PWM driver modules are combined onto a single 16 AWG trunk, which provides adequate margin for the expected current of approximately 8 A. Four such trunks then merge into a single 10 AWG main feed carrying about 32 A under nominal load. This value remains within the safe operating region for 10 AWG wire, providing sufficient thermal and electrical headroom. The entire system is supplied by a 24 V, 62.5 A power supply. Since the nominal system load is approximately 32 A, the supply operates with an electrical safety factor of about 1.95. This margin accommodates switching transients, uneven module usage, and simultaneous current draw across multiple sections of the array. It also ensures that the supply voltage remains stable during rapid duty-cycle updates, which contributes to consistent magnetic field generation and reliable control.

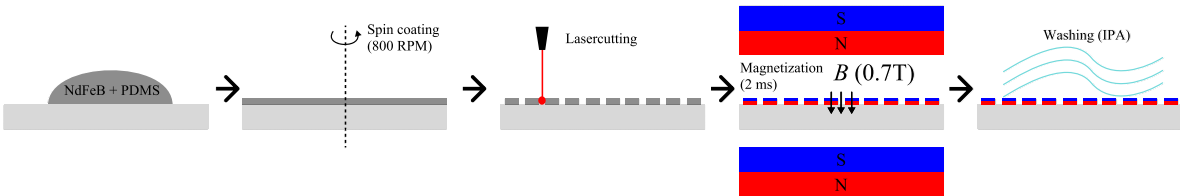


Figure 4: The microrobots are fabricated by spin-coating a 50 wt% NdFeB–silicone composite into a thin film ($\sim 100 \mu\text{m}$) and laser-cutting it into 3 mm disks. The cured disks are then magnetized in-plane using a custom fixture that generates a 0.7–0.9 T field, producing uniformly magnetized microrobots suitable for collective control experiments.

3.3 Microdisk fabrication

As shown in Fig. 4 we fabricate disk-shaped magnetic microrobots with a diameter of 3 mm and a thickness below 200 μm . A widely used method for creating soft magnetic actuators is to disperse hard-magnetic particles, such as NdFeB, within an elastomeric matrix. Following this approach, a

composite is prepared by mixing 50 wt% NdFeB microparticles with Smooth-SilTM 960 silicone. After thorough mixing and centrifuge-assisted degassing, the composite is spin-coated onto a circular acrylic at 800 rpm, producing a uniform film approximately 100 μm thick. This process ensures a consistently thin magnetic layer. During curing, UV illumination and mild heating at 60 °C are applied to accelerate cross-linking and prevent particle sedimentation, yielding homogeneous magnetic properties across the film. Once fully cured, the sheet is laser-cut into the desired microrobot geometry prior to magnetization.

3.4 Magnetizing

As shown in Fig. 4 each microrobot was magnetized in-plane with its magnetic orientation aligned along the thickness direction of the disk. Magnetization was performed by placing the cured microrobot sheet on a custom magnetization platform, where two permanent magnets were arranged in a sandwich configuration to generate a strong and uniform magnetic field. The magnetic flux density produced by this setup ranged from 0.7 T to 0.9 T, which was sufficient to fully magnetize the NdFeB–silicone composite for small batch fabrication. For future large-scale production, the same procedure will be carried out using a pulse magnetizer to achieve rapid and consistent magnetization across many microrobots.

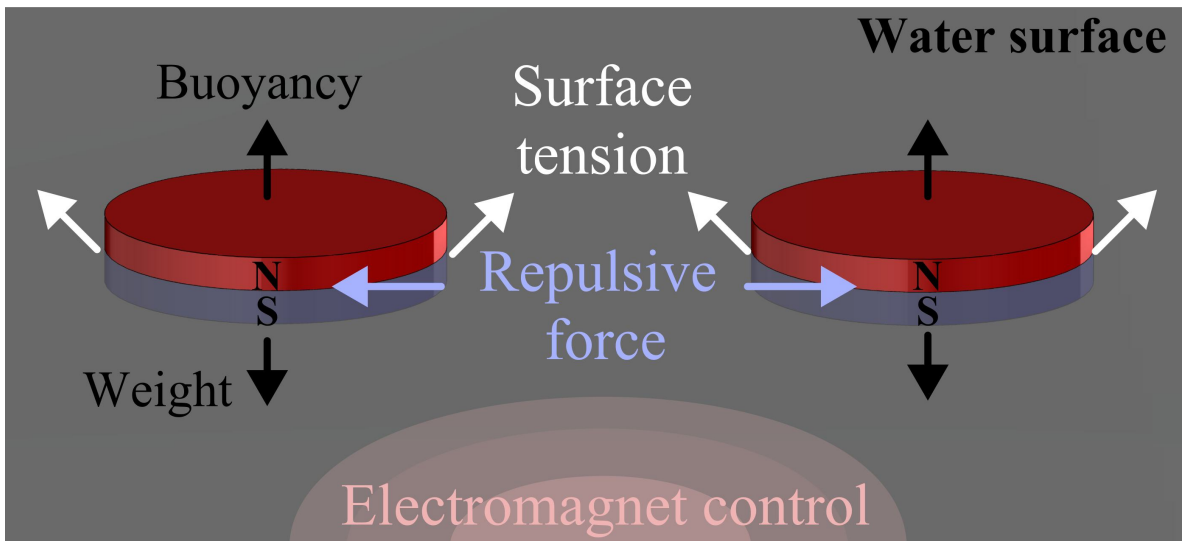


Figure 5: Forces acting between two vertically magnetized microrobots at the air–water interface. Each microrobot maintains an upright orientation due to surface-tension restoring forces, while buoyancy and weight remain balanced in the vertical direction. The figure illustrates the directions of the dominant forces, including magnetic dipole–dipole repulsion, capillary interaction, and externally applied magnetic forces. The equilibrium separation is reached when the horizontal external magnetic force is balanced by the combined magnetic and capillary repulsion, producing a stable two-robot spacing representative of larger swarm behavior.

3.5 Stabilizing microrobots at the air–water interface

As shown in Fig. 5, to ensure stable operation on the water surface, each microrobot is magnetized along its thickness direction. This orientation generates a vertical magnetic moment, and when multiple microrobots are activated together, the resulting dipole–dipole interactions remain predominantly repulsive. This repulsive interaction prevents clustering even when robots are pulled toward a target region by an external magnetic field.

Surface tension at the air–water interface plays a key role in stabilizing the robots. The interface constrains the microrobots to remain upright and provides a restoring force that balances vertical torques, ensuring that the magnetic moment remains aligned with the intended orientation. As the robots approach one another, the combination of repulsive magnetic forces and capillary interactions generates a well-defined equilibrium spacing, allowing the swarm to maintain a stable distributed configuration.

Under externally programmed magnetic fields, the microrobots move toward regions of lower magnetic potential energy. When they are far apart, their dynamics are dominated by the external field. When they become sufficiently close, inter-robot repulsion reshapes the total potential landscape, yielding stable lattice-like or formation-specific equilibria. This mechanism allows the swarm to form rings, lines, clusters with controlled spacing, or other user-defined formations without physical adhesion.

This principle follows the foundational theory established in prior work, where collective behavior on the air–water interface emerges from the balance between (i) externally applied magnetic forces, (ii) inter-modular magnetic repulsion, and (iii) capillary forces that stabilize orientation and resist vertical displacement. These interactions allow the swarm to remain spatially distributed while responding coherently to external magnetic actuation.

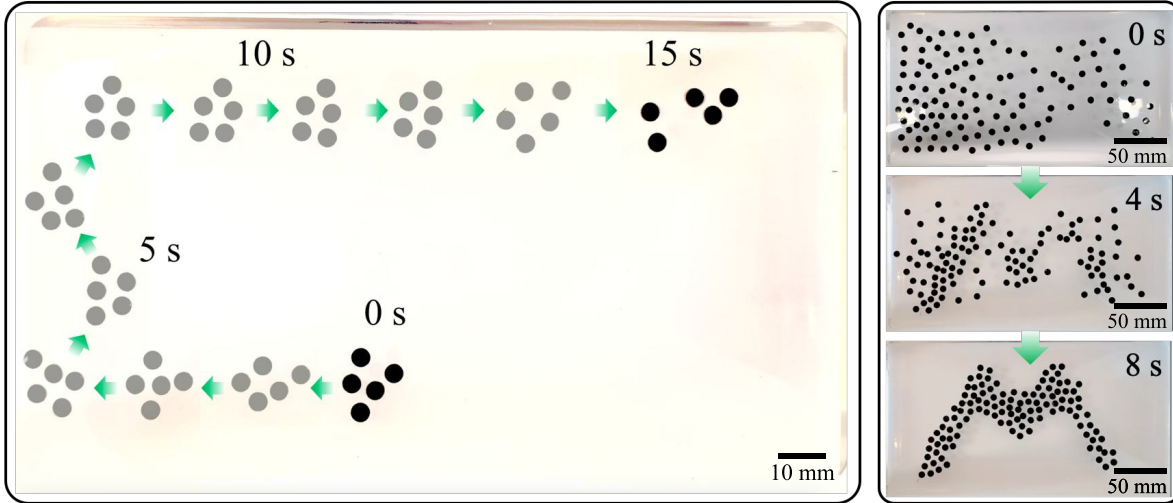


Figure 6: Demonstration of microrobot behavior prior to scaling to the full 1024-electromagnet array. Two experiments validate the core physical assumptions of the system: (1) whether the electromagnets can generate a sufficiently smooth magnetic potential landscape to drive multiple microrobots, and (2) whether vertically magnetized microdisks remain stable and maintain spacing at the air–water interface through surface tension and magnetic repulsion. In the first experiment, a swarm of five microdisks is translated for 15 s using programmed magnetic gradients, showing coherent motion and stable inter-robot spacing. In the second experiment, an “M”-shaped activation pattern is applied for 8 s, and the swarm reliably moves toward the induced potential minimum, confirming that localized magnetic inputs can shape collective motion.

4 Results

Using the developed electromagnetic control platform, we demonstrated stable manipulation and collective behaviors of microrobots at the air–water interface. Although the full system contains 1024 independently addressable electromagnets, the present experiments utilize a spatially contiguous quadrant of the array. This region provides sufficient magnetic resolution and workspace coverage to validate the physical interaction model, microdisk fabrication quality, and system-level actuation performance.

4.1 Collective stability governed by magnetic and capillary interactions

Figure 5 illustrates the dominant forces acting between two vertically magnetized microdisks at the fluid interface, including magnetic dipole–dipole repulsion, capillary stabilization, buoyancy, gravity, and externally applied magnetic gradients. Experiments confirmed that the fabricated microdisks naturally maintain upright orientations and preserve well-defined separation distances determined by the balance of these forces. This stable spacing enables collision-free collective motion even under spatially varying magnetic fields and forms the physical foundation for all subsequent swarm demonstrations.

4.2 Collective motion under spatially varying electromagnetic fields

By driving the active quadrant with programmable duty-cycle patterns, we generated smooth magnetic potential gradients that produced coherent swarm translation, rotation, and aggregation. The swarm moved toward commanded energy minima while maintaining lattice-like spacing due to persistent magnetic repulsion, consistent with the mechanics shown in Fig. 5. These behaviors validate that the electromagnetic array can shape the potential landscape with sufficient spatial resolution to control multiple agents simultaneously.

4.3 Trajectory shaping and pattern formation

Time-varying inputs allowed the high-level controller to sculpt the swarm trajectory within the quadrant. We observed elongated formations, contraction toward magnetic minima, and self-recentering behaviors as the potential landscape was modulated. Inter-robot repulsion ensured that these deformation modes proceeded smoothly without collapse, resulting in predictable collective responses suitable for higher-level coordinated tasks.

4.4 Validation of microdisk fabrication and magnetization

Uniformity of the NdFeB–silicone microdisks was validated experimentally. Magnetization using a 0.7–0.9 T in-plane field produced consistent dipole strengths, as reflected in nearly identical accelerations across robots subjected to the same magnetic inputs. This uniform response confirms that the fabrication process yields reproducible and reliable microrobots suitable for collective experiments.

4.5 Real-time response of the hardware platform

The partial electromagnet array enabled characterization of the full command pipeline. Quantized high-level commands were transmitted through USB, RS485, and dual I²C buses at update rates compatible with closed-loop control. Measured latencies closely matched the theoretical bounds, and the 24 V power network operated within safe thermal and electrical margins (safety factor ≈ 2). These tests verified that the system can sustain continuous real-time actuation of dense magnetic arrays without voltage droop or overheating.

4.6 Demonstration of programmable collective behaviors

Figure 7 summarizes the key experimental demonstrations enabled by the platform:

- **Object transport (Fig. 7a,c):** A swarm of microdisks encapsulated a PLA cargo disk and translated it across the workspace over 2 s. This motion was generated by spatially patterned activation of electromagnets within the quadrant of the 1024-element array, illustrating how localized actuation regions can induce coherent swarm-driven transport.
- **Swarmalator-inspired bouncing behavior (Fig. 7b):** Alternating activation and deactivation of local electromagnets induced rhythmic expansion–contraction dynamics, producing a bouncing-like collective motion. This demonstrates that temporal modulation of the magnetic landscape can shape coordinated multi-agent behaviors without requiring direct physical interactions.
- **Cargo encapsulation and propulsion (Fig. 7c):** Side and top views show the swarm forming a cohesive envelope around the cargo object and propelling it forward. The experiment highlights the combined effects of inter-robot repulsion, capillary alignment, and global magnetic guidance.

Together, Figs. 5 and 7 reveal that the fundamental physical stabilizing mechanisms of the microrobots directly enable functional swarm behaviors such as object transport and rhythmic motion generation.

These results demonstrate that even a quadrant of the full 1024-channel system provides sufficient spatial and temporal control authority to study and implement programmable microrobot collectives.

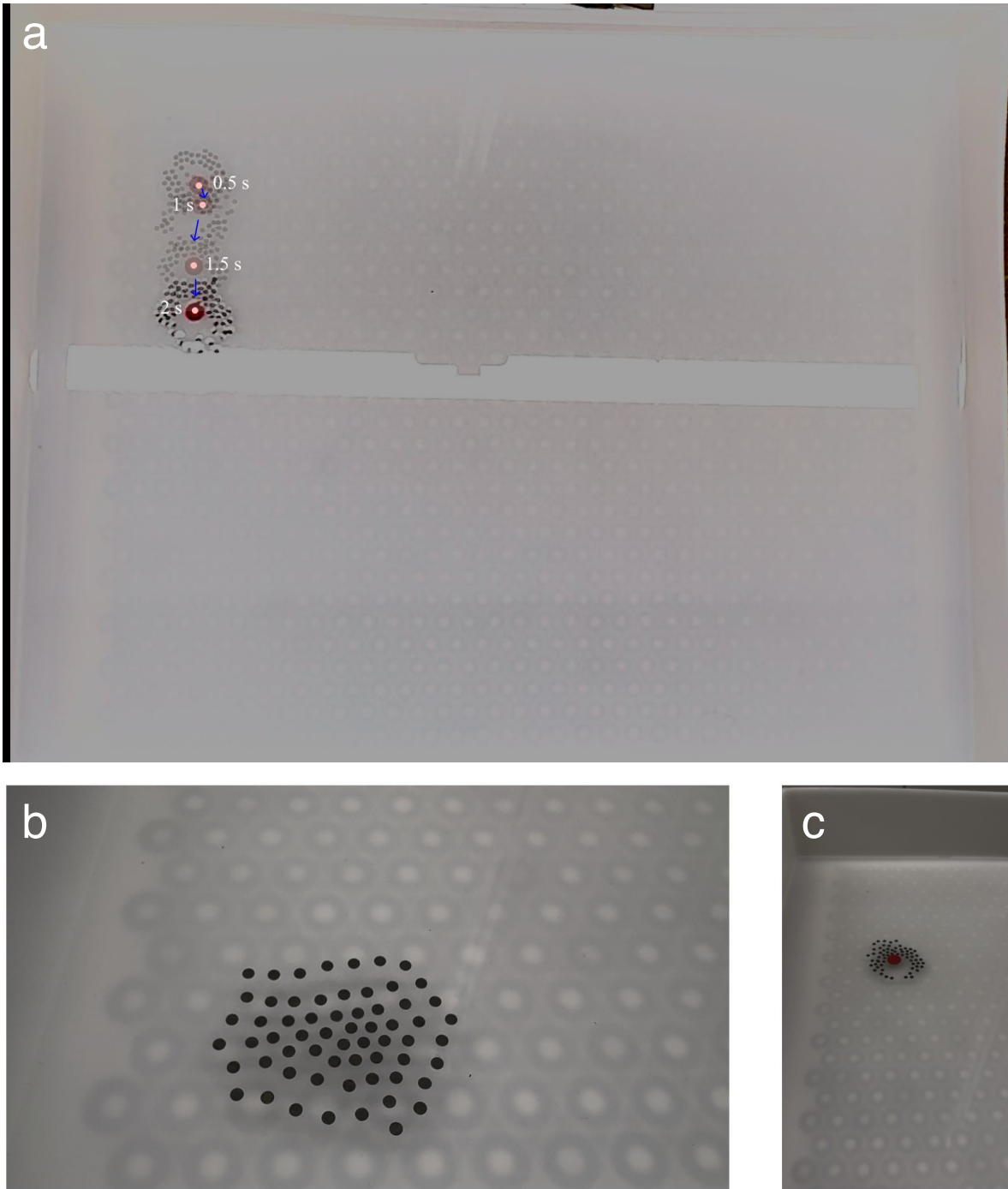


Figure 7: (a) Demonstration of object transport using a microrobot swarm. A PLA cargo disk (printed in red) is translated over a period of 2 s as the swarm pushes it forward, while the electromagnets beneath the workspace are activated with spatially patterned strengths to generate the required magnetic potential gradients. The experiment is performed on the full workspace located above the 1024-electromagnet array, illustrating how localized actuation regions within the larger field-of-view can drive coordinated swarm motion. (b) Illustration of the swarmalator-inspired bouncing behavior, achieved by alternately switching the electromagnets on and off to modulate local magnetic forces and induce rhythmic collective motion. (c) Side and top views of the transport experiment in (a), showing the swarm encapsulating the red cargo and propelling it forward as a cohesive unit.

5 Discussion

A substantial portion of this project was devoted to constructing the large-scale electromagnetic platform as shown in Fig. 8. Because the system requires assembling and wiring 1024 electromagnets, the hardware integration effort proved significantly more time-consuming than anticipated. The scale of the array, together with the need for safe and reliable power distribution, resulted in extended build times for cable routing, soldering, connector installation, and debugging. As a consequence, several planned experiments could not be completed within the semester.

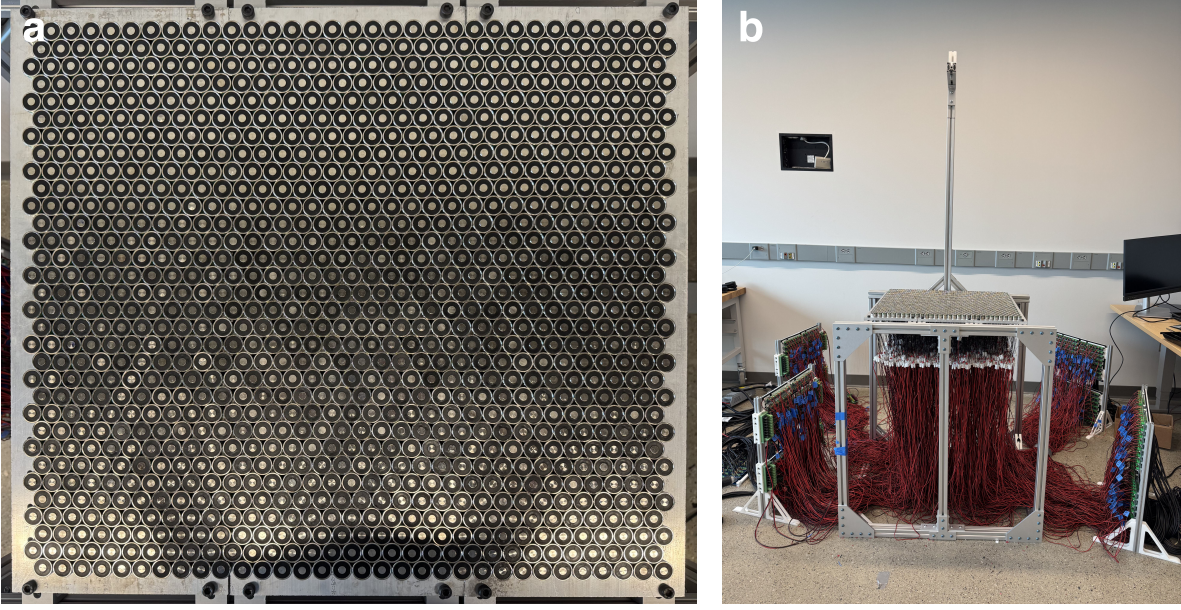


Figure 8: (a) Fully assembled array of 1024 electromagnets. (b) Completed experimental platform.

The next critical step is to incorporate an overhead vision system to extract quantitative measurements of the swarm state, including microrobot positions, velocities, and formation geometry. Reliable visual feedback is essential for closing the control loop and for validating collective behaviors at scale. Such measurements also form the foundation for connecting the platform to swarmalator-based models, where emergent patterns depend on parameters K and J that represent attractive and repulsive coupling strengths. To identify these mappings experimentally, a sufficiently large dataset must be collected under varying electromagnetic inputs, enabling the estimation of effective interaction laws between clusters.

Once accurate perception and interaction modeling are established, higher-level control strategies can be incorporated. Control barrier functions (CBFs) and control Lyapunov functions (CLFs) provide principled mechanisms for enforcing safety constraints, avoiding obstacles, encapsulating cargo, or transporting objects without collision. We envision developing these capabilities as a primary goal for the next stage of the platform, enabling structured manipulation tasks in addition to emergent pattern formation.

From a hardware perspective, several practical considerations must be addressed. Thermal management becomes increasingly important when operating many electromagnets simultaneously. Mounting a thermal camera above the array will enable real-time monitoring of temperature distribution and early detection of overheating. Additionally, parameters such as water height, microdisk diameter, and magnetization strength must be experimentally optimized. If inter-robot repulsion is too weak or too strong, control authority may degrade, leading to clustering or overly diffuse behavior. Identifying an optimal combination of geometry and magnetic moment is therefore essential for stable collective motion.

Beyond proof of concept, future work may explore increasing the complexity of individual microrobots. Although the present microdisks are deliberately simple, more advanced designs could integrate pas-

sive mechanical features, onboard sensing, or minimal embedded electronics. Such extensions would broaden the range of achievable behaviors and open new directions for multi-agent coordination at small scales.

Overall, the results of this project establish a foundation for high-density electromagnetic control of microrobot collectives. Completing perception integration, refining hardware design, and developing higher-level control policies will enable the platform to support richer studies in coordinated micro-robotics, swarm dynamics, and programmable active matter.

6 Budget

The budget and bill of materials were compiled based on the required items identified after October 6, as summarized in Table 1.

Table 1: Bill of Materials

Item	Description	Supplier	Unit (\$)	Qty	Total (\$)
Filament	Overture PLA	Overture	16.99	2	33.98
Silicone	Smooth-Sil 960 (2.2 lbs)	Reynolds Advanced Materials	42.50	1	42.50
Wire sleeving	1/8 in PET Braided Sleeving	Amazon	12.99	2	25.98
Wire	26 AWG Sil. Wire (250 ft)	BNTECHGO	18.48	3	55.44
Grand Total					157.90

References

- [1] M. Sitti, “Voyage of the microrobots,” *Nature*, vol. 458, no. 7242, pp. 1121–1122, 2009.
- [2] Q. Wang, J. Zhang, J. Yu, J. Lang, Z. Lyu, Y. Chen, and L. Zhang, “Untethered small-scale machines for microrobotic manipulation: From individual and multiple to collective machines,” *Acs Nano*, vol. 17, no. 14, pp. 13081–13109, 2023.
- [3] M. Sitti, H. Ceylan, W. Hu, J. Giltinan, M. Turan, S. Yim, and E. Diller, “Biomedical applications of untethered mobile milli/microrobots,” *Proceedings of the IEEE*, vol. 103, no. 2, pp. 205–224, 2015.
- [4] S. Palagi, A. G. Mark, S. Y. Reigh, K. Melde, T. Qiu, H. Zeng, C. Parmeggiani, D. Martella, A. Sanchez-Castillo, N. Kapernaum, *et al.*, “Structured light enables biomimetic swimming and versatile locomotion of photoresponsive soft microrobots,” *Nature materials*, vol. 15, no. 6, pp. 647–653, 2016.
- [5] V. Sridhar, B.-W. Park, and M. Sitti, “Light-driven janus hollow mesoporous tio2–au microswimmers,” *Advanced Functional Materials*, vol. 28, no. 25, p. 1704902, 2018.
- [6] H. Shahsavani, A. Aghakhani, H. Zeng, Y. Guo, Z. S. Davidson, A. Priimagi, and M. Sitti, “Bioinspired underwater locomotion of light-driven liquid crystal gels,” *Proceedings of the National Academy of Sciences*, vol. 117, no. 10, pp. 5125–5133, 2020.
- [7] D. Ahmed, T. Baasch, N. Blondel, N. Läubli, J. Dual, and B. J. Nelson, “Neutrophil-inspired propulsion in a combined acoustic and magnetic field,” *Nature communications*, vol. 8, no. 1, pp. 1–8, 2017.
- [8] M. Medany, L. Piglia, L. Achenbach, S. K. Mukkavilli, and D. Ahmed, “Model-based reinforcement learning for ultrasound-driven autonomous microrobots,” *Nature Machine Intelligence*, pp. 1–15, 2025.
- [9] S. Palagi and P. Fischer, “Bioinspired microrobots,” *Nature Reviews Materials*, vol. 3, no. 6, pp. 113–124, 2018.

- [10] X. Dong and M. Sitti, "Controlling two-dimensional collective formation and cooperative behavior of magnetic microrobot swarms," *The International Journal of Robotics Research*, vol. 39, no. 5, pp. 617–638, 2020.
- [11] W. Wang, V. Kishore, L. Koens, E. Lauga, and M. Sitti, "Collectives of spinning mobile microrobots for navigation and object manipulation at the air-water interface," in *2018 IEEE/RSJ International Conference on Intelligent Robots and Systems (IROS)*, pp. 1–9, IEEE, 2018.
- [12] D. Cappelleri, D. Efthymiou, A. Goswami, N. Vitoroulis, and M. Zavlanos, "Towards mobile microrobot swarms for additive micromanufacturing," *International Journal of Advanced Robotic Systems*, vol. 11, no. 9, p. 150, 2014.
- [13] Y. Kantaros, B. V. Johnson, S. Chowdhury, D. J. Cappelleri, and M. M. Zavlanos, "Control of magnetic microrobot teams for temporal micromanipulation tasks," *IEEE Transactions on Robotics*, vol. 34, no. 6, pp. 1472–1489, 2018.
- [14] G. T. Iványi, B. Nemes, I. Gróf, T. Fekete, J. Kubacková, Z. Tomori, G. Bánó, G. Vizsnyiczai, and L. Kelemen, "Optically actuated soft microrobot family for single-cell manipulation," *Advanced Materials*, vol. 36, no. 32, p. 2401115, 2024.
- [15] Z. Li, K. Wang, C. Hou, C. Li, F. Zhang, W. Ren, L. Dong, and J. Zhao, "Self-sensing intelligent microrobots for noninvasive and wireless monitoring systems," *Microsystems & Nanoengineering*, vol. 9, no. 1, p. 102, 2023.
- [16] F. Wang, E. Yildiz, X. L. Deán-Ben, Y. Yu, D. Nozdriukhin, W. Kang, S. Zhang, J. Zinnanti, D. Sheehan, R. H. Soon, *et al.*, "Optoacoustic-guided magnetic microrobot platform for precision drug delivery," *Advanced Materials*, p. e11870, 2025.
- [17] M. Z. Miskin, A. J. Cortese, K. Dorsey, E. P. Esposito, M. F. Reynolds, Q. Liu, M. Cao, D. A. Muller, P. L. McEuen, and I. Cohen, "Electronically integrated, mass-manufactured, microscopic robots," *Nature*, vol. 584, no. 7822, pp. 557–561, 2020.
- [18] J. Cheng, R. Zhang, H. Li, Z. Wang, C. Lin, P. Jin, Y. Nie, B. Lu, Y. Jiao, Y. Ma, *et al.*, "Soft crawling microrobot based on flexible optoelectronics enabling autonomous phototaxis in terrestrial and aquatic environments," *Soft Robotics*, vol. 12, no. 1, pp. 45–55, 2025.
- [19] S. Kim, A. M. Johnson, and S. Bergbreiter, "Picotaur: A 15 mg hexapedal robot with electrostatically driven, 3d-printed legs," *Advanced Intelligent Systems*, vol. 6, no. 10, p. 2400196, 2024.
- [20] Z. Zhakypov, K. Mori, K. Hosoda, and J. Paik, "Designing minimal and scalable insect-inspired multi-locomotion millirobots," *Nature*, vol. 571, no. 7765, pp. 381–386, 2019.
- [21] W. Hu, G. Z. Lum, M. Mastrangeli, and M. Sitti, "Small-scale soft-bodied robot with multimodal locomotion," *Nature*, vol. 554, no. 7690, pp. 81–85, 2018.
- [22] B. A. Grzybowski, H. A. Stone, and G. M. Whitesides, "Dynamic self-assembly of magnetized, millimetre-sized objects rotating at a liquid–air interface," *Nature*, vol. 405, no. 6790, pp. 1033–1036, 2000.
- [23] C. A. Aubin, R. H. Heisser, O. Peretz, J. Timko, J. Lo, E. F. Helbling, S. Sobhani, A. D. Gat, and R. F. Shepherd, "Powerful, soft combustion actuators for insect-scale robots," *Science*, vol. 381, no. 6663, pp. 1212–1217, 2023.
- [24] Y. Chen, H. Zhao, J. Mao, P. Chirarattananon, E. F. Helbling, N.-s. P. Hyun, D. R. Clarke, and R. J. Wood, "Controlled flight of a microrobot powered by soft artificial muscles," *Nature*, vol. 575, no. 7782, pp. 324–329, 2019.
- [25] X. Ji, X. Liu, V. Cacucciolo, M. Imboden, Y. Civet, A. El Haitami, S. Cantin, Y. Perriard, and H. Shea, "An autonomous untethered fast soft robotic insect driven by low-voltage dielectric elastomer actuators," *Science Robotics*, vol. 4, no. 37, p. eaaz6451, 2019.

- [26] Y. Lee, V. K. Bandari, J. S. McCaskill, P. Adluri, D. Karnaushenko, D. D. Karnaushenko, and O. G. Schmidt, “Si chiplet-controlled 3d modular microrobots with smart communication in natural aqueous environments,” *Science Robotics*, vol. 10, no. 105, p. eadu6007, 2025.
- [27] G. Gardi, S. Ceron, W. Wang, K. Petersen, and M. Sitti, “Microrobot collectives with reconfigurable morphologies, behaviors, and functions,” *Nature communications*, vol. 13, no. 1, p. 2239, 2022.
- [28] J. Yu, D. Jin, K.-F. Chan, Q. Wang, K. Yuan, and L. Zhang, “Active generation and magnetic actuation of microrobotic swarms in bio-fluids,” *Nature communications*, vol. 10, no. 1, p. 5631, 2019.
- [29] S. Ceron, K. O’Keeffe, and K. Petersen, “Diverse behaviors in non-uniform chiral and non-chiral swarmalators,” *Nature Communications*, vol. 14, no. 1, p. 940, 2023.
- [30] S. Ceron, G. Gardi, K. Petersen, and M. Sitti, “Programmable self-organization of heterogeneous microrobot collectives,” *Proceedings of the National Academy of Sciences*, vol. 120, no. 24, p. e2221913120, 2023.
- [31] X. Fan, X. Dong, A. C. Karacakol, H. Xie, and M. Sitti, “Reconfigurable multifunctional ferrofluid droplet robots,” *Proceedings of the National Academy of Sciences*, vol. 117, no. 45, pp. 27916–27926, 2020.